Electronic Supplementary Material (ESI) for Journal of Materials Chemistry A.

Supporting Information

Quantitative Probing of Available Extra Capacity: Interfacial Space-Charge Storage in FeOOH Lithium-ion Battery

Leqing Zhang,[a†] Zeyuan Bu,[a†] Haoyu Fu,[a] Xiaoshan Wang,[a*] Xianyi Meng,[a] Meishuo Liu,[a] Yakun Zhou,[a] Xiang Sui,[a] Guihuan Chen,[a] Qinghao Li,[a] Qiang Li,*[ab]

[a] College of Materials Science and Engineering, College of Physics, Weihai Innovation Research Institute, Qingdao University, Qingdao 266071, China.

[b] Department of Electrical and Computer Engineering & Institute for Quantum Computing, University of Waterloo, Ontario N2L 3G1, Canada.

† These authors contributed to this work equally.

*** Corresponding author, E-mail addresses: liqiang@qdu.edu.cn; wangxiaoshan1@qdu.edu.cn**

Contents

Calculated section

Section I. Langevin fitting of superparamagnetic magnetization

The saturation magnetization of superparamagnetic particles can be obtained by Langevin function:

$$M(H,T) = M_s L\left(\mu_p H / k_B T\right) \quad (S1)$$

In equation (S1), M_s is the saturation magnetization, $L(x) = \coth x - (1/x)$, μ_p is the magnetic moment per particle, k_B is the Boltzmann constant, T is the temperature constant 300K. By fitting the magnetic hysteresis loop of Figure 2c, we found that the saturation magnetization of the FeOOH electrode is 84.01 emu g^{-1} after discharge to 0.01 V, and the average diameter of Fe grains is 2.6 nm.

Section II. The interfacial spin-polarized charge storage *Q* quantified by the change of magnetization

ΔM: $\Delta M = \frac{3.6 \times Q}{e} \times p \times \mu_B$, where p is effective spin polarization of -37% ~ -45%, e is constants of 1.6 × 10^{-19} C, μ_B is the Bohr magneton 9.274 × 10^{-21} emu.

Section III. Thermodynamics modeling for interfacial space charge storage

Based on Gauss' law, the Li-excess regime is as follows for the concentration of conduction electrons n between 3 and 4:

$$exp\left(-\frac{eE}{k_B T}\right) \propto Q^n exp(\gamma Q) \quad (S5)$$

Where e, k_B and T represents the charge quantity per electron, Boltzmann constant and temperature, respectively. The relationship between voltage E and the charge per mass of composites Q can be obtained as shown in Figure 3d. According to the dominant factors, it can be divided into two areas, small Q (high voltages area) and large Q (low voltages area). Therefore, the equation (S5) can be divided into two parts:

For small Q:
$$-\frac{eE}{k_B T} = n \ln Q \quad (S6)$$

For large Q:
$$-\frac{eF(Q,E)}{k_B T} = \gamma Q \quad (S7)$$

$$F(Q,E) = [E + n\frac{k_B T}{e} \ln Q] \quad (S8)$$

For the high voltage range in Figure 3d, the fitting slope was obtained by equation (S6) within small Q area, and n = 3.125. Then, for the low voltage range which abides by equations (S7, S8), the relationship of $F(Q,E)$ and Q are exhibited Figure 3e. The fitting γ value with the boundary condition (n = 3 or 4) is on the order of 1, close to the theoretical value of the space charge storage dominant mechanism.

Section IV. Calculation of Li^+ diffusion coefficient in Galvanostatic intermittent titration techniques (GITT)

The Li^+ diffusion coefficient D_{Li^+} can be calculated by the following formula:

$$D_{Li^+} = \frac{4}{\pi\tau}\left(\frac{m_B V_m}{M_B S}\right)^2\left(\frac{\Delta E_s}{\Delta E_\tau}\right)^2 \qquad (S2)$$

Where τ is the constant current pulse time, m_B,V_m, M_B, S,ΔE_s and ΔE_τ represent the mass of active material, the molar volume of active material, the molar mass of active material, the electrode surface area, steady state voltage variation and temporary voltage variation during constant current pulse mode. The GITT pulse time and relaxation time were set to 10 min.

Section V. The fitting of pseudo-capacitance capacity

The contribution of diffusion-controlled and capacitive capacity can be divided by equation (S3):

$$i = k_1 v + k_2 v^{1/2} \qquad (S3)$$

Where i is the current at a fixed potential V and v is the scan rate in the CV tests. The value of $k_1 v$ and $k_2 v^{1/2}$ represents surface pseudo-capacitance and diffusion-controlled contribution, respectively. Here, we fitted k_1 and k_2 at all potentials and calculated the proportion of capacity shown in Figure S13.

Section VI. The fitting of pseudo-capacitance capacity and calculation of the b value

The electrochemical reaction kinetics can be further analyzed by the b value in the following equation:

$$i = av^b \qquad (S4)$$

The b value can be fitted by the current i at a fixed potential V and the scan rate v, b = 0.5 represents diffusion-limited behavior, 1.0 represents surface-controlled capacitive behavior.

Section VII. The reaction equation during the discharging process in Figure 3f

Step I: $FeOOH + xLi^+ + xe^- \rightarrow Li_xFeOOH$

Step II: $Li_xFeOOH + yLi^+ + ye^- \rightarrow Li_{x+y}FeOOH$

Step III: $zLi_{x+y}FeOOH + zLi^+ + ze^- \rightarrow Fe + Li_2O + LiOH$, $x + y + z = 3$

Step III'+II'+I': $Fe + (n/3)Li_2O + (n/3)LiOH \rightarrow Li_nFeOOH$, $0 < n < 3$

Section VIII. Curie-Weiss fitting and ion content analysis

The magnetic susceptibility χ of a paramagnetic material follows the equation:

$$\frac{1}{\chi} = \frac{(T-\theta)}{C} \qquad (S5)$$

Where *C* is the Curie constant, *T* is the temperature, and θ is the Curie-Weiss temperature. Hence, the Curie constant can be obtained by linearly fitting the obtained $\frac{1}{\chi}$.

The effective magnetic moment, μ_{eff}, can be calculated through the Curie constant C:

$$C = \frac{N\mu_0\mu_{eff}^2}{3k_B} \qquad (S6)$$

Where *N* represents the number (number density) of magnetic ions per unit volume. μ_0 refers to the magnetic permeability of the vacuum. μ_{eff} is the effective magnetic moment. k_B stands for the Boltzmann constant. The total effective magnetic moment can be expressed as the square root of the sum of the squares of all individual ionic magnetic moments. Based on calculations involving high-spin Fe^{2+} (with an effective magnetic moment of 4.899 μ_B) and low-spin Fe^{3+} (with an effective magnetic moment of 1.732 μ_B), the respective percentages are determined to be 42.3% and 57.7%.

Supplementary Figures and Table

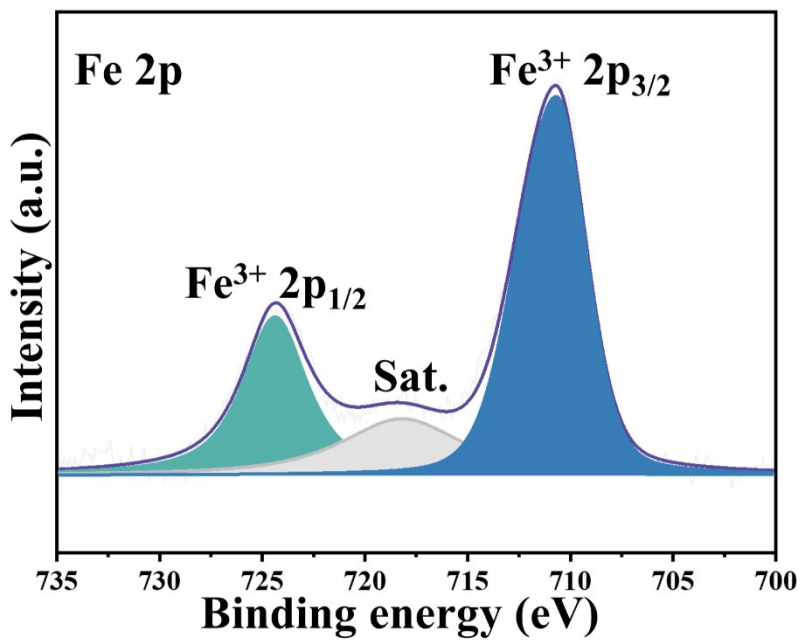

Figure S1. High-resolution X-ray photoelectron spectroscopy (XPS) spectra of the Fe 2p regions of the FeOOH electrode.

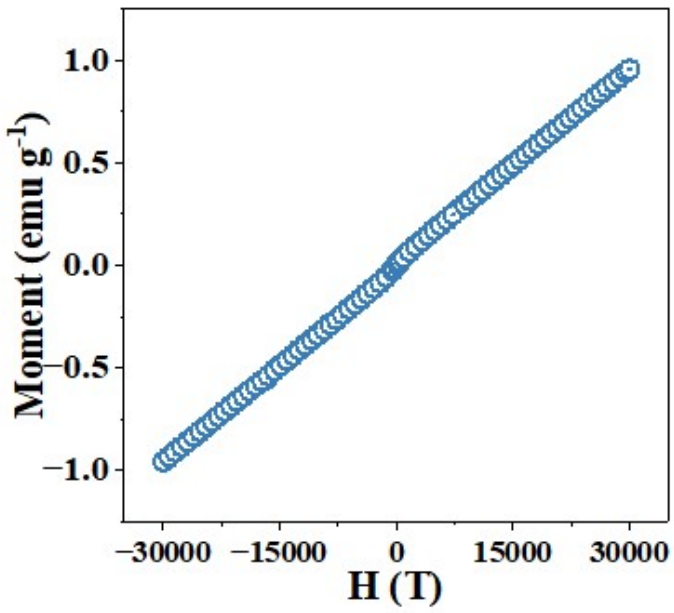

Figure S2. Magnetic hysteresis (MH) loop of FeOOH sample measured at 300 K.

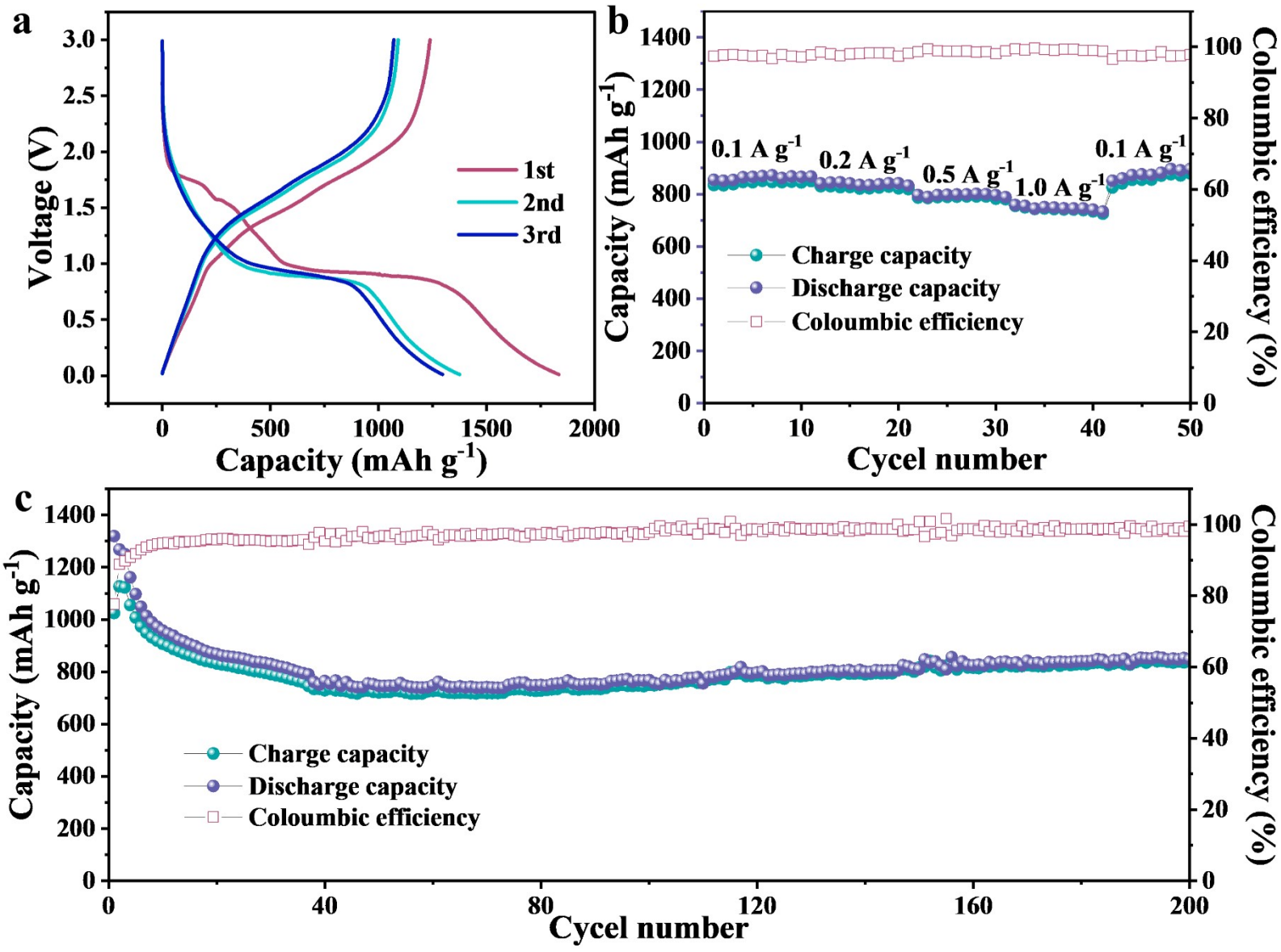

Figure S3. a) Galvanostatic charge-discharge for the first three cycles of FeOOH LIBs in the potential window of 0.01-3 V at 0.1 A g^{-1}. b) Rate performance at different current densities. c) Cycle performance at 0.2 A g^{-1} for 200 cycles.

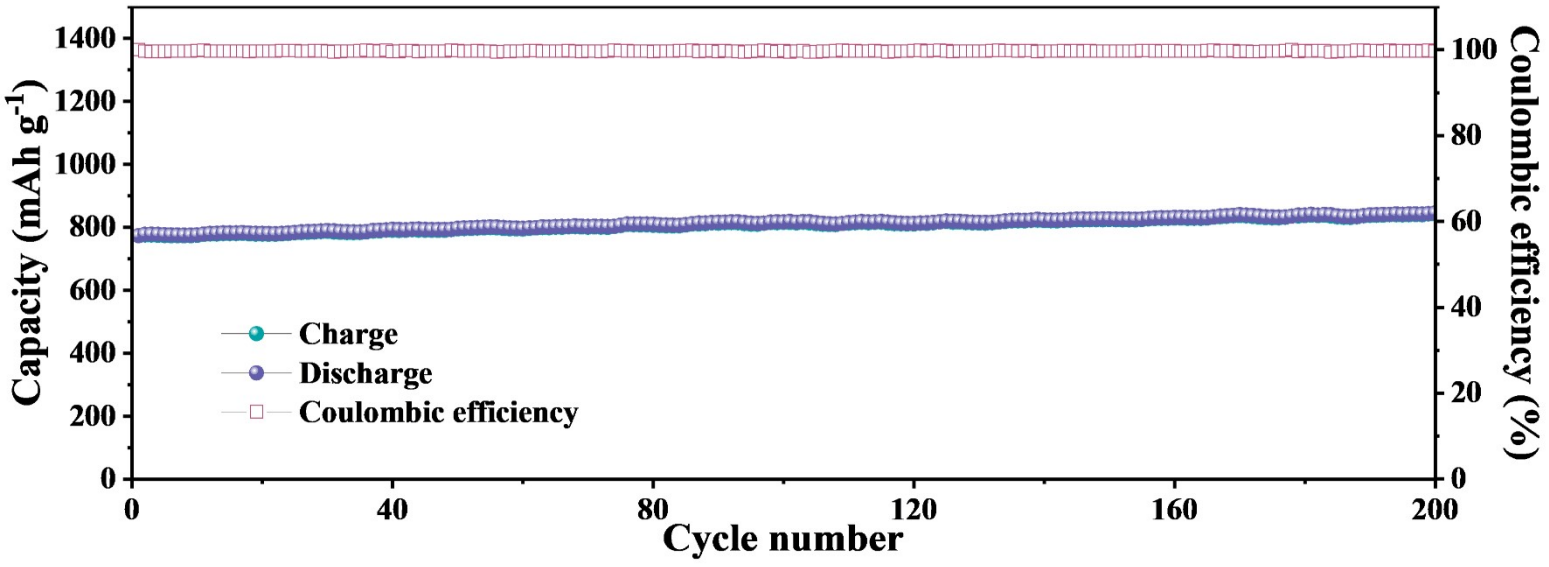

Figure S4. Long cycle performance of FeOOH LIBs at 1 A g^{-1}.

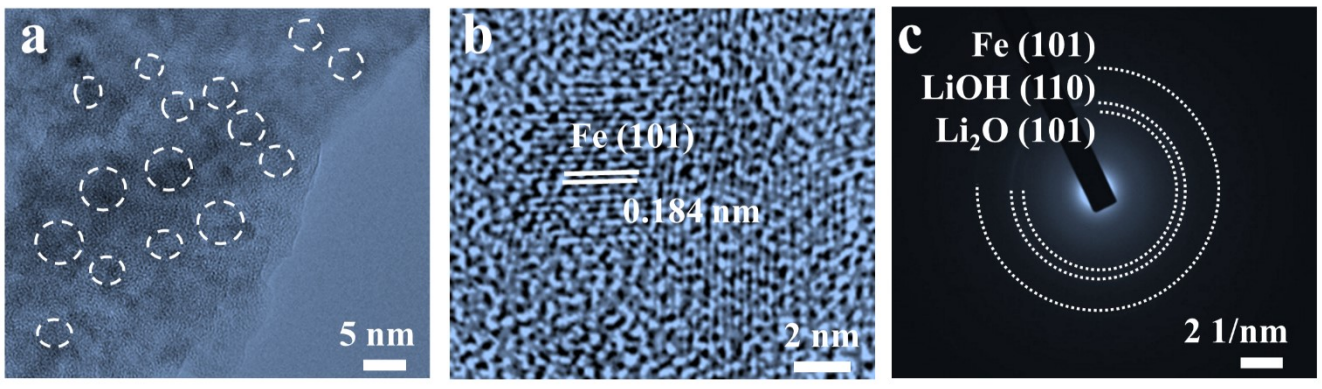

Figure S5. a) TEM image of FeOOH electrode after first discharge to 0.01 V. b) High-resolution HRTEM image showing the presence of Fe and Li_2O/LiOH after the first discharge. c) SAED pattern of reaction products after first discharge to 0.01 V.

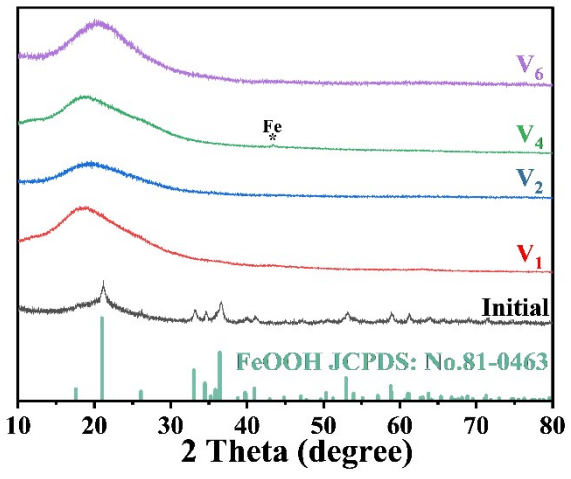

Figure S6. Quasi-in-situ XRD patterns of the electrodes at different lithiation states. The voltage legends are consistent with the voltage shown in Figure 2b.

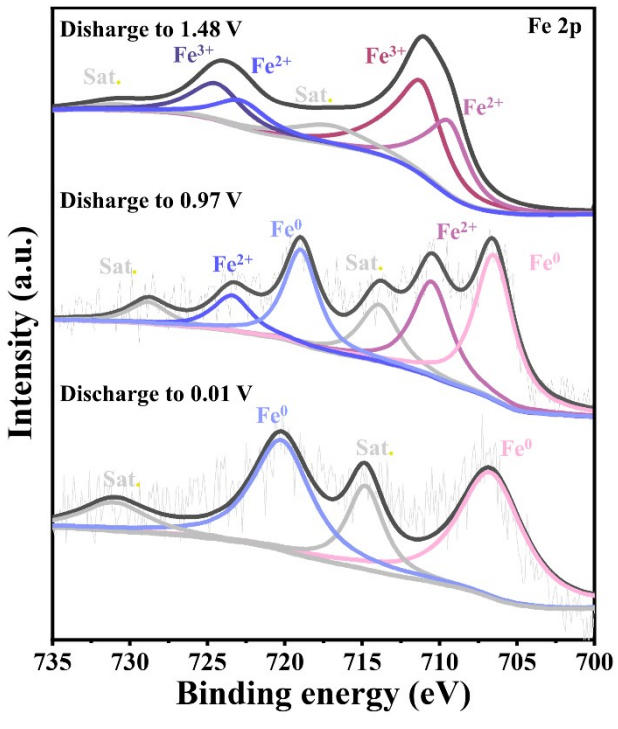

Figure S7. XPS patterns of the Fe 2p across various discharge steps.

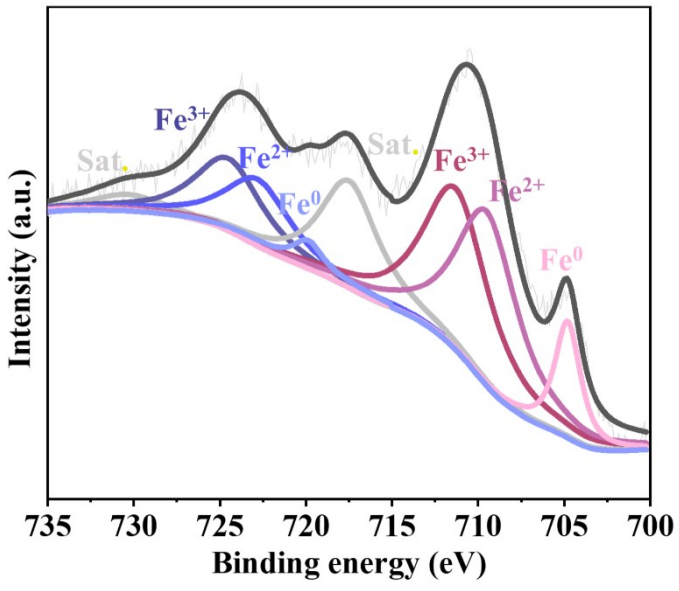

Figure S8. XPS patterns of the Fe 2p after the first cycle.

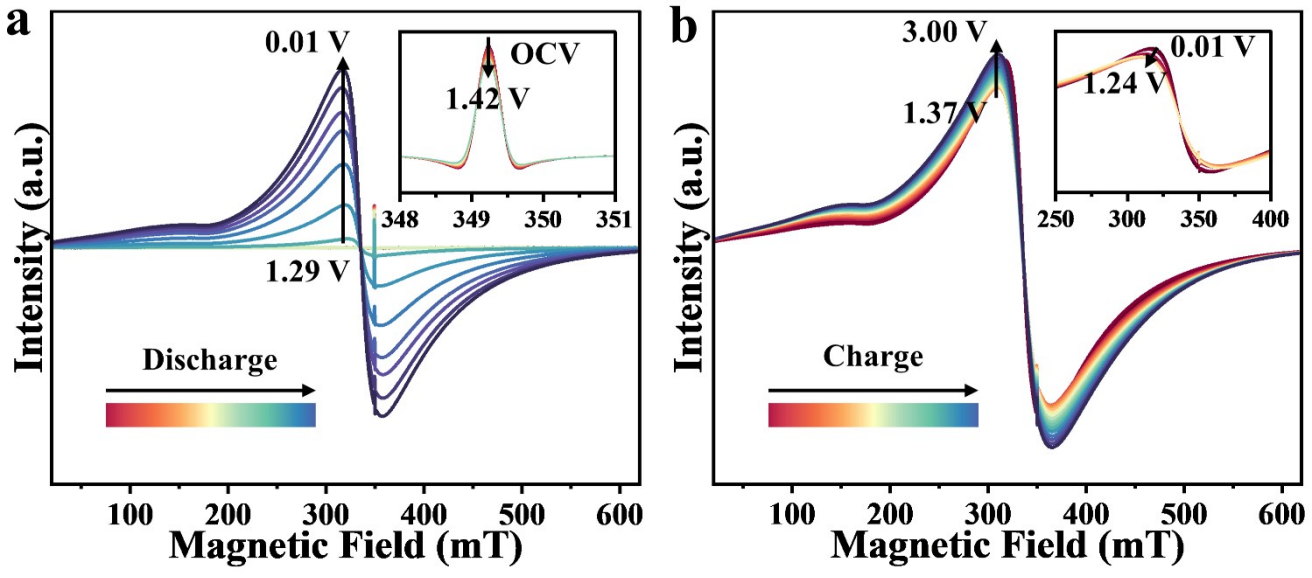

Figure S9. In situ EPR spectra during a) discharging and b) charging processes.

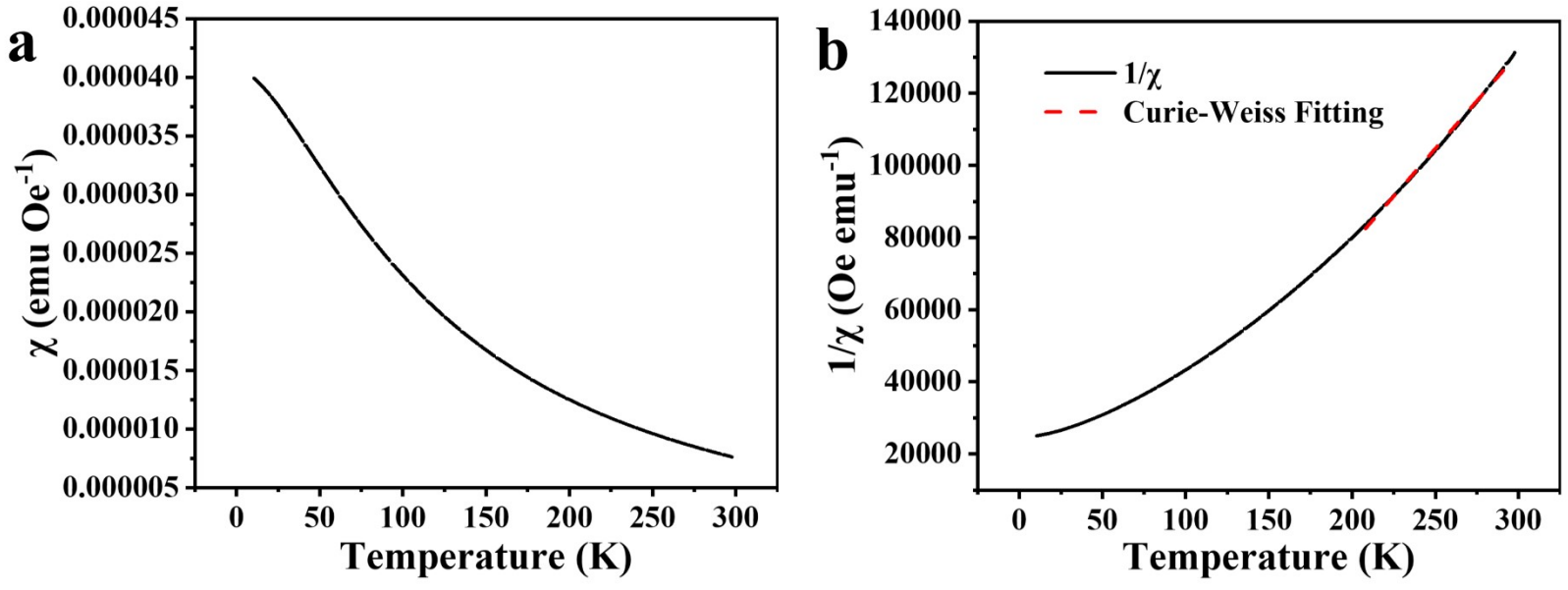

Figure S10. a) χ-T curves of FeOOH after the first cycle. b) 1/χ curves of FeOOH after the first cycle and Curie Weiss Fitting.

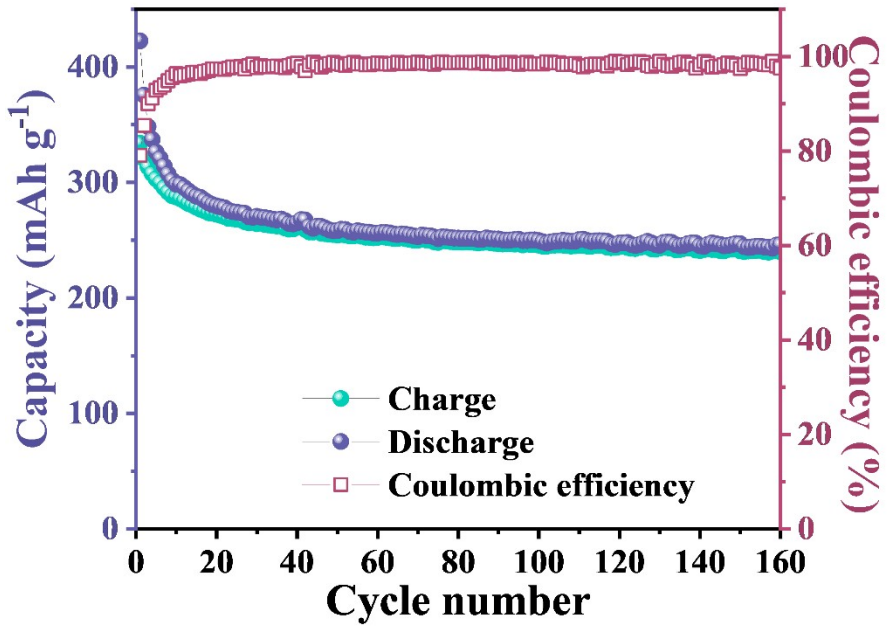

Figure S11. Cycling performance of FeOOH LIBs at a current density of 0.1A g^{-1} in the potential window of 0.01-1 V.

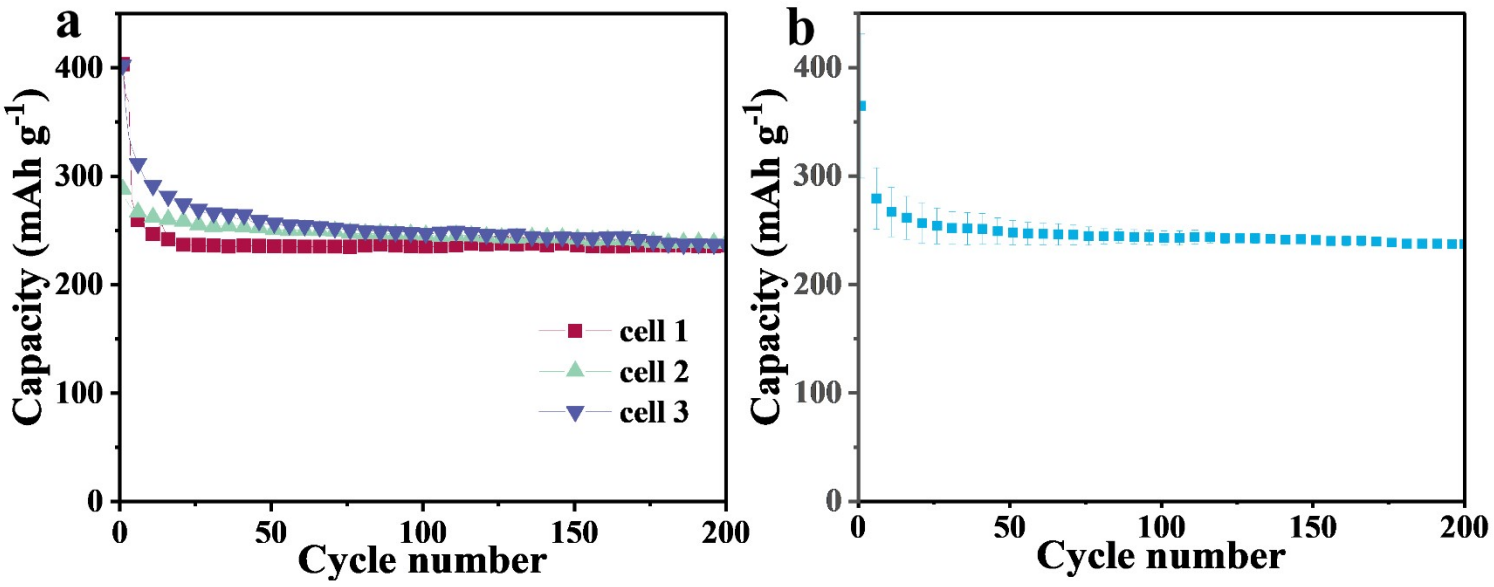

Figure S12. a) Comparison of discharge capacity of different batteries. b) Capacity error diagram of different batteries, the central bar indicates the mean, and the error bar indicates standard error.

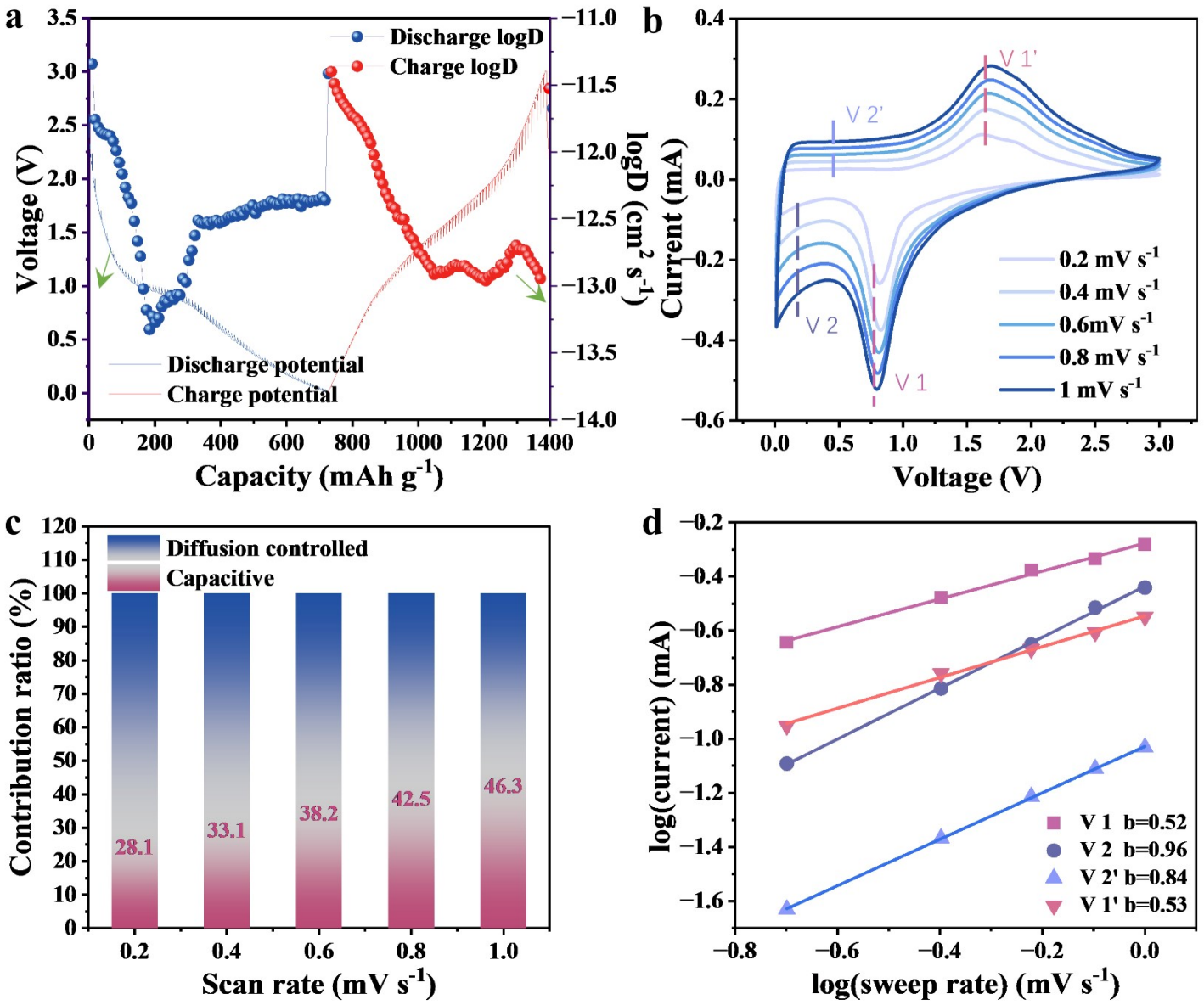

Figure S13. a) GITT measurements on α-FeOOH LIBs during the first cycles. b) The CV curves at various scan rates from 0.2 to 1 mV s^{-1}. c) Normalized contribution ratio of diffusion-controlled and capacitive capacities at different scan rates. d) Determination of the b value at the typical potentials shown in b).

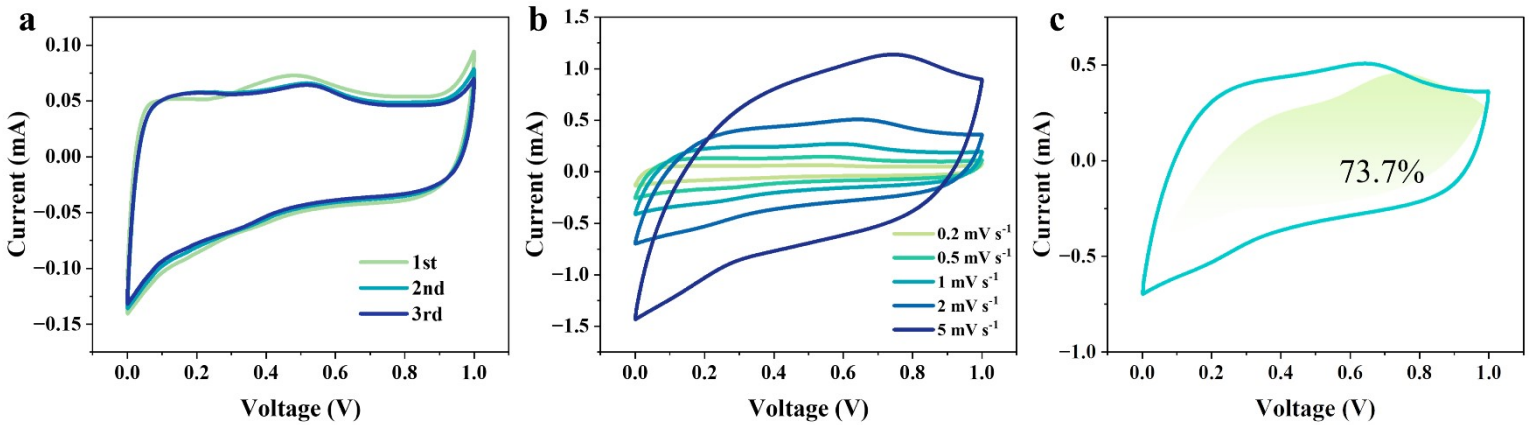

Figure S14. a) The CV curves of FeOOH LIBs at a scan rate of 0.2 mV s^{-1} in the potential window of 0.01-1 V. b) The CV curves at various scan rates from 0.2 to 5 mV s^{-1}. (c) Capacitive contributed to charge storage at a scan rate of 5 mV s^{-1}.

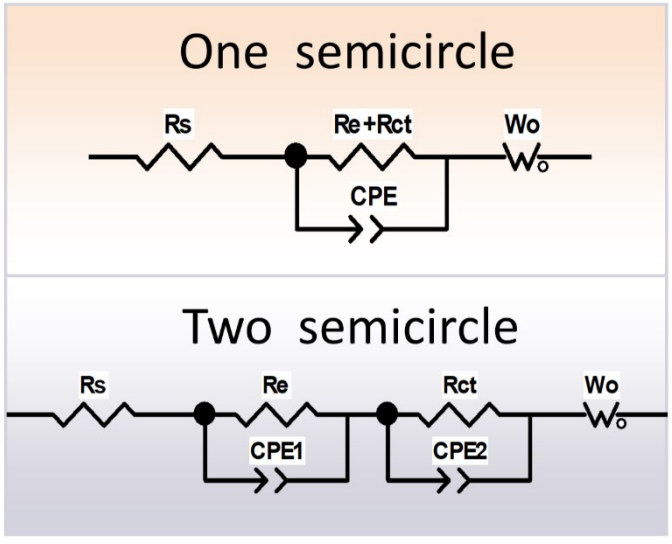

Figure S15. The equivalent circuit pattern.

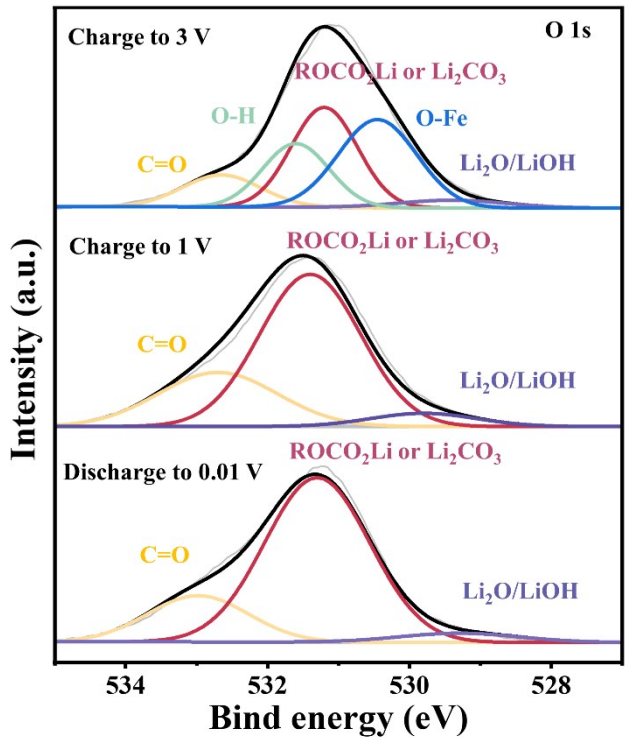

Figure S16. XPS patterns of the O 1s at different voltages.

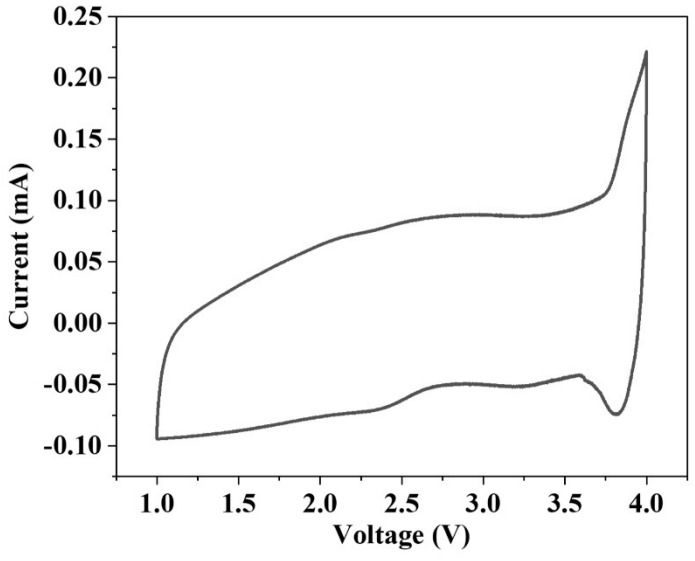

Figure S17. The CV curves of FeOOH-reduced//AC LIC in the range of 1-4 V.

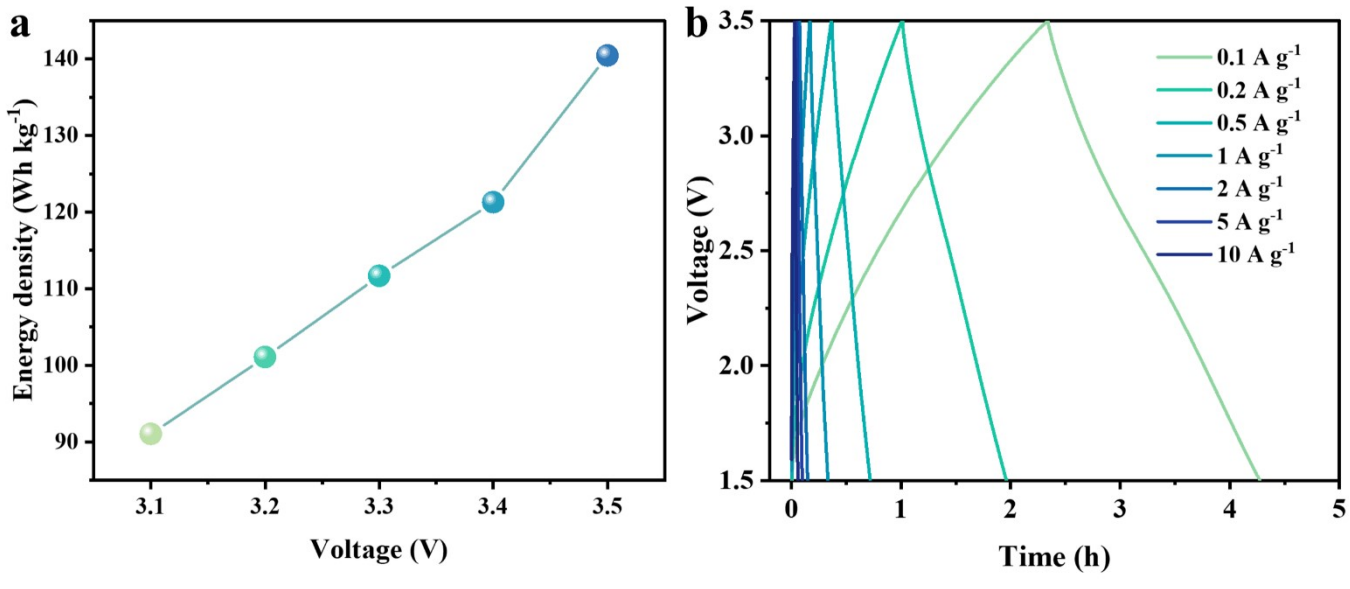

Figure S18. a) Energy density of the LICs with the increase in the voltage window at a fixed current density of 0.2 A g^{-1}. b) Galvanostatic charge-discharge curves at various current densities in FeOOH-reduced//AC LIC.

Table S1. Comparison of electrochemical performance for LICs.

LICs	E (V)	Energy density (Wh Kg^{-1})	Cycle number (I mA g^{-1})	Capacity retention (%)	Ref.
This work	1.5-3.5	140.44	1000 (1000)	99.6	-
Fe_2O_3//AC	0-3.4	90	2500 (150)	55	1
$CoSe_2$@NC //AC	1.0-4.2	130	8000 (5000)	90.8	2
$CoSe_2$/N-rGO//AC	1.0-4.2	104.2	8000 (1000)	81.2	3
Co_3O_4@TiO_2//AC	0.5-4.0	87.9	6000 (500)	88.1	4
Fe_3O_4@C//AC	0-4.0	110.1	1000 (1000)	95.7	5
$TiSe_2$@CSA //AC	0-4.2	96.7	4000 (5000)	80.9	6
$FeSe_2$/$CoSe_2$ @NGC//AC	0-4.0	106.31	1400 (2000)	90	7
T-Nb_2O_5/rGO //AC	1.0-4.2	123.7	20000 (5000)	83.6	8
pTi_3C_2/C-2//AC	0.1-4.2	110.0	2000 (2000)	80	9
ω-$Li_3V_2O_5$//AC	1.0-4.0	117.9	2500 (1000)	96.3	10
$Nb_{12}O_{29-x}$@C//AC	0.01-3.5	72.4	500 (200)	80	11

References

1 **A. Brandt and A. Balducci, *Electrochim. Acta*, 2013, 108, 219-225.**

2 **L. Wang, X. Zhang, Y. Kong, C. Li, Y. An, X. Sun, K. Wang and Y. Ma, *Rare Metals*, 2024, 43, 2150-2160.**

3 **W. Wei, L. Wang, C. Liang, W. Liu, C. Li, Y. An, L. Zhang, X. Sun, K. Wang, H. Zhang, X. Zhang and Y. Ma, *Chem. Eng. J.*, 2023, 474, 145788.**

4 **Y. Peng, H. Liu, Y. Li, Y. Song, C. Zhang and G. Wang, *J. Colloid Interf. Sci.*, 2021, 596, 130-138.**

5 **C. Han, L. Xu, H. Li, R. Shi, T. Zhang, J. Li, C. Wong, F. Kang, Z. Lin and B. Li, *Carbon*, 2018, 140, 296-305.**

6 **Z. Bo, Z. Zheng, Y. Huang, Z. Huang, P. Chen, J. Yan, K. Cen, H. Yang and K. K. Ostrikov, *Chem. Eng. J.*, 2023, 473, 145183.**

7 **S. Tao, J. Cai, Z. Cao, B. Song, W. Deng, Y. Liu, H. Hou, G. Zou and X. Ji, *Adv. Energy Mater.*, 2023, 13, 2301653.**

8 **L. Wang, X. Zhang, C. Li, Y. Xu, Y. An, W. Liu, T. Hu, S. Yi, K. Wang, X. Sun, Y. Gong, Z. Wu and Y. Ma, *Chem. Eng. J.*, 2023, 468, 143507.**

9 **H. Zhou, L. Lin, Z. Sui, H. Wang and B. Han, *Acs Appl. Mater. Inter.*, 2023, 15, 12161-12170.**

10 **X. Lan, X. Liu, T. Meng, S. Yang, Y. Shen and X. Hu, *Small Methods*, 2023, 7, 2201290.**

11 **C. Liu, B. Wang, L. Xu, K. Zou, W. Deng, H. Hou, G. Zou and X. Ji, *Acs Appl. Mater. Inter.*, 2023, 15, 5387-5398.**